Progress In Electromagnetics Research B, Vol. 44, 261–282, 2012

ELECTROMAGNETIC FIELD OF ARBITRARILY ORIENTED COIL ANTENNAS IN COMPLEX UNDERGROUND ENVIRONMENT

N. Yuan[1, *], R. Liu[1], and X. Nie[2]

[1]Department of Electrical and Computer Engineering, University of Houston, 4800 Calhoun Road, Houston, TX 77204, USA

[2]Sensor Physics & Technology — Halliburton, 3000 N. Sam Houston Pkwy E, Houston, TX 77032, USA

Abstract—In this paper, a finite-difference based method is presented to simulate the electromagnetic field generated by arbitrarily-oriented coil antennas in three-dimensional (3-D) complex underground media. The media have multiple layers in both the vertical and horizontal direction and can be fully anisotropic. The developed finite-difference method uses a staggered grid to approximate a vector equation in terms of the scattered electric field. The resultant linear sparse matrix is solved iteratively using a generalized minimal residual (GMRES) algorithm and an incomplete LU precondition technique is applied to improve the convergence behavior of the linear equation, thus accelerate the solution. The developed algorithm is validated by numerical examples and then applied to the simulation and study of the popular triaxial induction tools in electrical well logging engineering for anisotropy detection.

1. INTRODUCTION

Study of electromagnetic field generated by coil antennas in complex underground environment is very important in geophysical exploration. As we know, hydrocarbon (oil or gas) reservoir has high resistivity/low conductivity compared to other non-reservoir rocks. Thus from the resistivity profile of an underground formation, geologists can determine reservoir layers and hydrocarbon contents in the rock. The resistivity profile of an underground formation is usually obtained from its electromagnetic (EM) field response of the electrical

Received 23 July 2012, Accepted 13 September 2012, Scheduled 27 September 2012

* Corresponding author: Ning Yuan (nyuan@uh.edu).

logging tools. These days, as thick-layered hydrocarbon reservoirs are gradually getting exhausted, detection and exploration of thin laminated reservoirs are becoming more and more important. Thin laminated sand-shale reservoirs usually demonstrate anisotropy in electric properties, characterized by the horizontal and vertical resistivity/conductivity. Detection of the electrical anisotropy of geologic formations is a problem that has attracted the attention of geophysicists for nearly 70 years [1]. The recently developed triaxial induction tools can detect the anisotropy of the media. In the tool, the transmitters and receivers are small coil antennas oriented at orthogonal directions. The anisotropic media respond to different components of the transmitter–receiver combinations, therefore the tool is able to measure formation resistivities with anisotropy. For faithful interpretation of data acquired in complex geologic settings, it is critical to accurately predict the behavior of induced electromagnetic (EM)response of these coil antennas in three-dimensional (3-D) geometries comprising borehole, invasions in the horizontal direction and multiple layers in the vertical direction. Efficient solution of Maxwell's equations in such 3-D anisotropic media is still a challenging problem and receives increasing interests. Existing 3-D EM modeling techniques applied in well logging problems include finite-element techniques [2–5], integral equation method [6–8], finite-difference methods [9–15], the closely related finite-volume method [16, 17] etc.. Each kind of method has its own advantages and disadvantages. Among these methods, finite-element methods are most flexible in modeling complicated geometry. However they are not as straightforward to implement as finite-difference methods. Integral equation method can be highly efficient for relatively simple models, but their computational complexity and memory requirement increase quickly with the increase of cell numbers. The recently developed fast algorithms [8] alleviate this problem by speeding up the solution and reducing the memory storage but the method is still restricted to isotropic media. Finite-difference methods are simple in concept and straightforward in implementation. Various techniques have been developed to make the method more efficient and flexible, making the method one of the most popular techniques in the geophysical EM simulations.

In this paper, we present a finite-difference based simulation method to calculate the electrical and magnetic fields resulting from an inductive source embedded in a 3D fully anisotropic medium. The generalized anisotropy of the medium is described by a symmetric 3×3 tensor. In this algorithm, we use an edge-centered, staggered-grid finite difference method to solve the Maxwell's equations in the quasi-static

frequency domain. An averaged conductivity tensor [10] is used for each cell so that relatively coarser mesh can be used. The generalized minimized residual (GMRES) [18] is used to solve the resultant matrix equation and the incomplete LU (ILU) precondition [19, 20] is applied to improve the convergence property of the equation. The developed code is very efficient and it enables simultaneous multi-spacing and multi-frequency computing of the tool responses to arbitrary 3D anisotropic formations.

This paper is organized as follows. First, we derive the governing partial differential equation (PDE) which describes low-frequency EM induction in anisotropic media. Then, the finite-difference method for staggered grids is used to solve the governing PDE. The detailed finite-difference equation for a fully anisotropic formation is presented. In the numerical results section, some examples are presented to demonstrate the efficiency and capability of the present method. Then the method is applied to study the EM response of a triaxial induction tool which comprises three orthogonal transmitter coils and three orthogonal receiver coils in 3-D anisotropic media.

2. FORMULATION

2.1. Governing Equations

Consider an infinitely small arbitrarily oriented coil antenna located in a multi-layered anisotropic media, as shown in Figure 1.

The governing equations for EM induction in the 3-D geometry

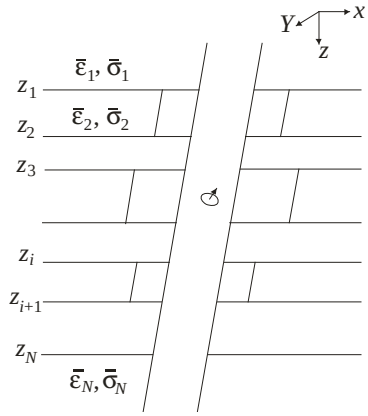

Figure 1. A coil antenna in an underground multi-layered anisotropic media.

are Faraday's law and Ampere's law

$$\nabla \times \mathbf{E} = -i\omega \mathbf{B} \tag{1a}$$

$$\nabla \times \mathbf{H} = \mathbf{J}_i + \mathbf{J}_s + i\omega \mathbf{D} \tag{1b}$$

where $\mathbf{J}_s$ is the source current density and $\mathbf{J}_i$ is the induced current density. In the above equations, a time-harmonic dependence of $e^{i\omega t}$ is assumed and suppressed. The induced current density $\mathbf{J}_i$ is related to the electric field by

$$\mathbf{J}_i = \bar{\sigma}\mathbf{E} \tag{2}$$

The total electric field $\mathbf{E}$ can be expressed as the sum of a primary field $\mathbf{E}_0$ from $\mathbf{J}_s$ embedded in a background reference medium and a scattered field $\mathbf{E}'$ arising from the conductivity and permittivity variations which deviate from the background medium. In geophysical applications, we usually prefer a scattered-field formulation instead of a total-field one since the former computations are more robust and accurate, particularly when the measurements are made very close to the source. A total-field solution usually requires very fine meshes, resulting in large demands of computational resources. In addition, it is impossible to obtain accurate in-phase responses from the total-field solution since the direct-coupled field is dominant in the total field.

Setting $\mathbf{E} = \mathbf{E}'$ in (1) and combining (1)–(3) yield a single, second order partial-differential equation (PDE) in terms of the scattered electric field:

$$\nabla \times \nabla \times \mathbf{E}' + i\omega\mu_0 \left(\bar{\sigma} + i\omega\varepsilon\right) \mathbf{E}' = -j\omega\mu_0 \mathbf{J}_0 \tag{3}$$

The term $\mathbf{J}_0$ is the effective source current density for the scattered fields,

$$\mathbf{J}_0 = \left[\left(\bar{\sigma}\left(\mathbf{r}\right) - \sigma_0 \mathbf{I}\right) + j\omega\left(\varepsilon\left(\mathbf{r}\right) - \varepsilon_0\right)\mathbf{I}\right]\mathbf{E}_0 \tag{4}$$

where $\mathbf{I}$ is the 3×3 identity matrix. It is noted that both the conductivity and permittivity are position-dependant and can be fully anisotropic, i.e.,:

$$\bar{\sigma}\left(\mathbf{r}\right) = \begin{bmatrix} \sigma_{xx} & \sigma_{xy} & \sigma_{xz} \\ \sigma_{yx} & \sigma_{yy} & \sigma_{yz} \\ \sigma_{zx} & \sigma_{zy} & \sigma_{zz} \end{bmatrix}, \quad \bar{\varepsilon}\left(\mathbf{r}\right) = \begin{bmatrix} \varepsilon_{xx} & \varepsilon_{xy} & \varepsilon_{xz} \\ \varepsilon_{yx} & \varepsilon_{yy} & \varepsilon_{yz} \\ \varepsilon_{zx} & \varepsilon_{zy} & \varepsilon_{zz} \end{bmatrix} \tag{5}$$

2.2. Finite-difference Solution

Next, we use the finite-difference method based on the staggered Yee grid [21] to solve (3). The solution domain is discretized into Cartesian cells and the scattered electric field components E_x, E_y and E_z are defined on the edges of the cells. The magnetic-field component H_x is staggered in y and z, H_y in x and z, and H_z in x and y, as shown in Figure 2.

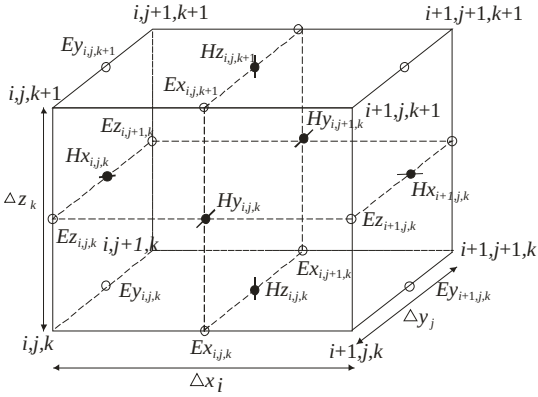

Figure 2. The staggered grid used for the finite-difference method.

Combining (3) and (4) and expanding the curl operations yield the following coupled expressions for the scattered electric field:

$$\begin{aligned}
&\frac{\partial}{\partial y}\left(\frac{\partial \mathbf{E}_y^s(\mathbf{r})}{\partial x}-\frac{\partial \mathbf{E}_x^s(\mathbf{r})}{\partial y}\right)-\frac{\partial}{\partial z}\left(\frac{\partial \mathbf{E}_x^s(\mathbf{r})}{\partial z}-\frac{\partial \mathbf{E}_z^s(\mathbf{r})}{\partial x}\right)\\
&\quad+j\omega\mu_0\left(\sigma_{xx}(\mathbf{r})\,\mathbf{E}_x^s(\mathbf{r})+\sigma_{xy}(\mathbf{r})\,\mathbf{E}_y^s(\mathbf{r})+\sigma_{xz}(\mathbf{r})\,\mathbf{E}_z^s(\mathbf{r})\right)\\
&=-j\omega\mu_0\left(\sigma(\mathbf{r})-\sigma_0(\mathbf{r})\right)\mathbf{E}_x^b(\mathbf{r})\\
&\frac{\partial}{\partial z}\left(\frac{\partial \mathbf{E}_z^s(\mathbf{r})}{\partial y}-\frac{\partial \mathbf{E}_y^s(\mathbf{r})}{\partial z}\right)-\frac{\partial}{\partial x}\left(\frac{\partial \mathbf{E}_y^s(\mathbf{r})}{\partial x}-\frac{\partial \mathbf{E}_x^s(\mathbf{r})}{\partial y}\right)\\
&\quad+j\omega\mu_0\left(\sigma_{yx}(\mathbf{r})\,\mathbf{E}_x^s(\mathbf{r})+\sigma_{yy}(\mathbf{r})\,\mathbf{E}_y^s(\mathbf{r})+\sigma_{yz}(\mathbf{r})\,\mathbf{E}_z^s(\mathbf{r})\right)\\
&=-j\omega\mu_0\left(\sigma(\mathbf{r})-\sigma_0(\mathbf{r})\right)\mathbf{E}_y^b(\mathbf{r})\\
&\frac{\partial}{\partial x}\left(\frac{\partial \mathbf{E}_x^s(\mathbf{r})}{\partial z}-\frac{\partial \mathbf{E}_z^s(\mathbf{r})}{\partial x}\right)-\frac{\partial}{\partial y}\left(\frac{\partial \mathbf{E}_z^s(\mathbf{r})}{\partial y}-\frac{\partial \mathbf{E}_y^s(\mathbf{r})}{\partial z}\right)\\
&\quad+j\omega\mu_0\left(\sigma_{zx}(\mathbf{r})\,\mathbf{E}_x^s(\mathbf{r})+\sigma_{zy}(\mathbf{r})\,\mathbf{E}_y^s(\mathbf{r})+\sigma_{zz}(\mathbf{r})\,\mathbf{E}_z^s(\mathbf{r})\right)\\
&=-j\omega\mu_0\left(\sigma(\mathbf{r})-\sigma_0(\mathbf{r})\right)\mathbf{E}_z^b(\mathbf{r})
\end{aligned}\tag{6}$$

In this paper, a 13-point centered finite-difference stencil [10] is used to approximate the curl-curl operator in (3). The above differential equation is converted to a linear system equation as follows,

$$\mathbf{KE}=\mathbf{S}\tag{7}$$

where the matrix $\mathbf{K}$ is the system matrix of dimension $3N_xN_yN_z \times 3N_xN_yN_z$ for a model with $3N_xN_yN_z$ cells. $\mathbf{E}$ is a vector of length $3N_xN_yN_z$ containing the secondary electric filed values E_x^s, E_y^s, E_z^s for all nodes. $\mathbf{S}$ (length $3N_xN_yN_z$) is the secondary-source vector given

by the right-hand side of (6). The system matrix $\mathbf{K}$ is a sparse matrix with up to 13 nonzero entries per line. The entries depend on the grid spacing and the frequency-dependent properties of the media.

In the derivation of the linear equations, a conductivity averaging scheme is used to obtain the conductivity at the center of the cell edge (where the electric field is defined). Following the scheme in [10], the conductivity at the center of the edge is expressed as a weighted sum of the conductivities of the four adjoining cells. The Dirichlet condition is applied to the scattered electric field components on the outmost boundary of the finite-difference mesh. The detailed expression of the matrices can be found in the Appendix. It should be noted that the system equation is non-symmetric originally. By multiplying (A1) by $\Delta x_{i+1/2}\Delta y_j\Delta z_k$, (A2) by $\Delta x_i\Delta y_{j+1/2}\Delta z_k$, and (A3) by $\Delta x_i\Delta y_j\Delta z_{k+1/2}$, we can obtain the symmetric form of the system equation, where Δx_i, Δy_j, Δz_k are the length of grid cells i, j, and k; $\Delta x_{i+1/2}$, $\Delta y_{j+1/2}$ and $\Delta z_{k+1/2}$ are the distances between the centers of cells $i+1$ and i, $j+1$ and j, and $k+1$ and k, respectively.

The linear system in (7) is solved efficiently using a generalized minimal residual (GMRES) algorithm [18] and the incomplete LU preconditioner (ILU) [19, 20] is used to improve the convergence of the matrix equation. Once the electric field is obtained from Equation (7), the magnetic field can be calculated from Faraday's law

$$\mathbf{H}=\frac{1}{-j\omega\mu}\left[\left(\frac{\partial E_z}{\partial y}-\frac{\partial E_y}{\partial z}\right)\hat{\mathbf{x}}+\left(\frac{\partial E_x}{\partial z}-\frac{\partial E_z}{\partial x}\right)\hat{\mathbf{y}}+\left(\frac{\partial E_y}{\partial x}-\frac{\partial E_x}{\partial y}\right)\hat{\mathbf{z}}\right]. \quad (8)$$

In the implementation, the partial derivatives in (8) are replaced by the corresponding differences that can be computed by interpolating the electric field to the observation points and several vicinity points.

Equation (7) usually converges slow, especially when the conductivity contrast in the formation is large. To overcome this difficulty, we use an incomplete LU preconditioner (ILU) to improve the convergence property of the matrix equation [19, 20].

2.3. Electromagnetic Field Response of Triaxial Induction Tools

Solving (3), we can obtain the scattered field. Then the total field is the sum of the primary field and the scattered field. Equation (3) is valid for transmitter coils oriented at arbitrary direction. For a triaxial induction tool as shown in Figure 3(a), it usually comprises three orthogonal transmitter coils and three orthogonal receiver coils, as shown in Figure 3(b). Since the transmitter coils are infinitely small, it can be treated as an equivalent magnetic dipole oriented at

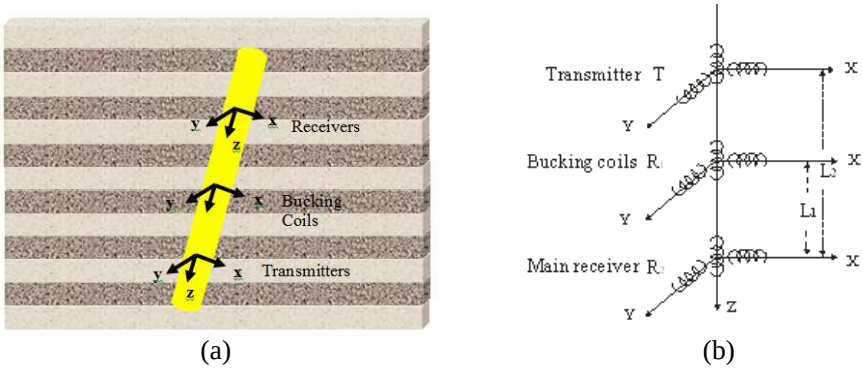

Figure 3. A triaxial induction tool and its general coil structure. (a) A triaxial induction tool in an anisotropic formation. (b) The general coil structure of an induction tool.

the normal direction to the coil surface. The magnetic dipole source $\mathbf{M} = (M_x, M_y, M_z)$ are characterized by the source current $I(\omega)$ as

$$\mathbf{M} = -j\omega\mu_0 I(\omega)\mathbf{a}\delta(r - r_s) \tag{9}$$

where r_s is the position of the transmitter coil, $\mathbf{a} = (a_x, a_y, a_z)$ are the areas of the current-carrying loop projected into the (y, z), (x, z), and (x, y) planes, respectively. The primary fields generated by the transmitter coil are computed in a homogeneous background medium with the conductivity and permittivity given at the source point. The total radiation field of the tilted coil is the summation of the fields from the x-directed, y-directed and z-directed components of the source. For the homogeneous background model, explicit expressions for the EM fields in the frequency domain can be derived.

2.4. Averaged Conductivity Tensor

Since the underground formation we consider is usually very complicated, including the borehole, dipping beds, invasions and anisotropic media, a fine mesh is necessary to model the complicated structures and interfaces between different media. However, a fine mesh requires large computer resource. A feasible way to alleviate this difficulty is to use reasonably coarse mesh to model the geometry and use the averaged conductivity for each cell to model the electrical property of the media. This is a good compromise between accuracy and computational complexity. So in most cases, the grid used in the finite-difference method is independent on the electrical property of the formation and different media can be included in a single rectangular

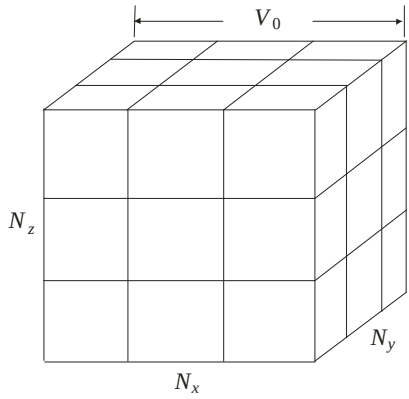

Figure 4. Partitioning of a cell for calculating the average conductivity tensor.

cell by using the averaged conductivity. In this paper, a technique similar to the one described in [10] is used to calculate the average conductivity tensor.

We consider a generalized anisotropic medium, whose conductivity is described by a symmetric 3×3 tensor given in (5). To derive the averaged conductivity tensor for each rectangular cell, the cell is first divided into $N_x \times N_y \times N_z$ subcells in the Cartesian coordinate system, as shown in Figure 4. Each subcell is assumed to have a constant conductivity tensor denoted by $\bar{\bar{\sigma}}^{(i,j,k)}$. Without loss of generality, we consider the derivation of the entries $\langle \sigma_{xx} \rangle$ and $\langle \sigma_{yx} \rangle$ of the averaged conductivity, other entries can be obtained following a similar procedure. To derive $\langle \sigma_{xx} \rangle$, we apply a voltage V_0 across the cell in the x-direction, as shown in Figure 4. By assuming the electric field to be uniform across each subcell and the electric current continuous across the subcell boundaries vertical to the x-direction, we can write out the x-directed electric field $E_x^{(i,j,k)}$ in each subcell as

$$E_x^{(i,j,k)} = \frac{N_x}{\sum\limits_{i'=1}^{N_x} \left(\sigma_{xx}^{(i,j,k)} / \sigma_{xx}^{(i',j,k)} \right)} V_0 / \Delta x. \tag{10}$$

The average x-directed current density for the cell can be expressed as a summation of the densities of all the subcells with the

same superscript i. If we choose $i = 1$, the average current is,

$$\langle J_x \rangle = \frac{\sum_{j=1}^{N_y} \sum_{k=1}^{N_z} \sigma_{xx}^{(1,j,k)} E_x^{(1,j,k)}}{N_y N_z} \tag{11}$$

Then the average conductivity entry $\langle \sigma_{xx} \rangle$ be written as,

$$\langle \sigma_{xx} \rangle = \langle J_x \rangle / (V_0/\Delta x) = \frac{\sum_{j=1}^{N_y} \sum_{k=1}^{N_z} \left(N_x / \sum_{i'=1}^{N_x} \left(1/\sigma_{xx}^{(i',j,k)} \right) \right)}{N_y N_z} \tag{12}$$

Equation (12) implies that the averaged conductivity $\langle \sigma_{xx} \rangle$ is obtained by first combining in series the N_x subcells with the same superscript i in a line and then combining in parallel the $N_x \times N_y$ lines of subcells.

Next, we derive the expression of the off-diagonal entry $\langle \sigma_{yx} \rangle$. For a generalized anisotropic medium, the conductivity $\sigma_{yx}^{(i,j,k)}$ of each subcell is non-zero, which means that any voltage applied in the x-direction may cause a current flowing in the y-direction. The current density J_y in each subcell due to E_x is given by

$$J_y^{(i,j,k)} = \sigma_{yx}^{(i,j,k)} E_x^{(i,j,k)} \tag{13}$$

The average y-directed current density is the average of those of all the $N_x \times N_y \times N_z$ subcells, that is

$$\langle J_y \rangle = \frac{\sum_{i=1}^{N_x} \sum_{j=1}^{N_y} \sum_{k=1}^{N_z} \sigma_{yx}^{(i,j,k)} E_x^{(i,j,k)}}{N_x N_y N_z} \tag{14}$$

Substituting (15) into (14), the average conductivity $\langle \sigma_{yx} \rangle$ can be obtained by,

$$\langle \sigma_{yx} \rangle = \langle J_y \rangle / (V_0/\Delta x) = \frac{\sum_{i=1}^{N_x} \sum_{j=1}^{N_y} \sum_{k=1}^{N_z} \sigma_{yx}^{(i,j,k)} \left(1/ \sum_{i'=1}^{N_x} \left(\sigma_{xx}^{(i,j,k)} / \sigma_{xx}^{(i',j,k)} \right) \right)}{N_y N_z} \tag{15}$$

Following the above procedure, we can derive other average conductivity entries $\langle \sigma_{yy} \rangle$, $\langle \sigma_{zz} \rangle$, $\langle \sigma_{xz} \rangle$ and $\langle \sigma_{yz} \rangle$. To preserve the symmetric character of the average conductivity tensor, we set the average conductivity entries $\langle \sigma_{\alpha\beta} \rangle$ to be the average of the calculated $\langle \sigma_{\alpha\beta} \rangle$ and $\langle \sigma_{\beta\alpha} \rangle$, that is

$$\langle \sigma_{\alpha\beta} \rangle = \langle \sigma_{\beta\alpha} \rangle = \frac{1}{2} \left(\langle \sigma_{\alpha\beta} \rangle + \langle \sigma_{\beta\alpha} \rangle \right) \quad \alpha = x, y, z \quad \beta = x, y, z \quad \alpha \neq \beta \tag{16}$$

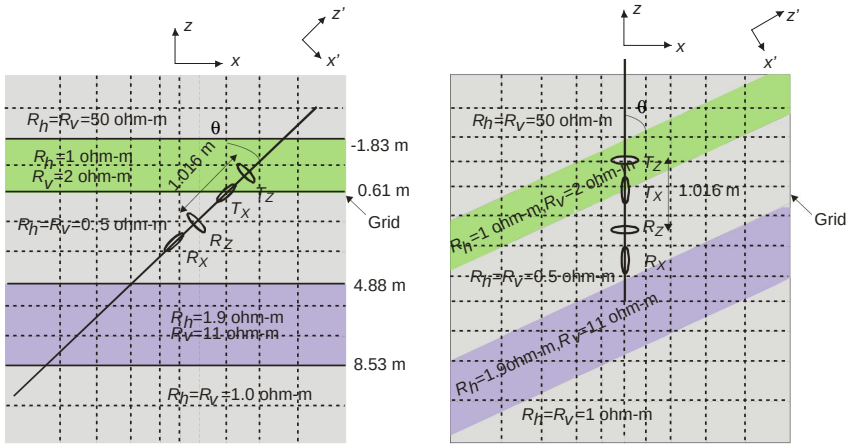

Figure 5. Two models constructed for an internal consistency check. (a) Model 1. (b) Model 2.

3. NUMERICAL RESULTS

Based on the above theory, we developed a code to simulate the electromagnetic field response of arbitrarily oriented coil antennas in complicated anisotropic media and further extended it to the simulation of triaxial induction tool responses. To validate the code, we first present an internal consistency check.

Consider a 1-D layered structure as shown in Figure 5. Layer 1, 3 and 5 are isotropic media with resistivity of 50 ohm-m, 0.5 ohm-m and 1.0 ohm-m, respectively. Layer 2 is anisotropic medium and has a vertical resistivity of 11 ohm-m and a horizontal resistivity of 1.9 ohm-m. Layer four has a vertical resistivity of 2.0 ohm-m and a horizontal resistivity of 1.0 ohm-m. The depth of each layer is shown in the figure. In the fist model, we assume the principal axes of the resistivity tensor of the media coincide with the x-y-z coordinate system and the transmitter and receiver coils are tilted 60°, as shown in Figure 5(a). In the second model, we tilt the principal axes of the media and aligning the source in the z-direction while the multi-layered formation is tiled in the x'-y'-z' reference frame, as shown in Figure 5(b). The two models are expected to give the same results although the implementation of the codes are different, thus providing an internal consistency check for the developed code.

In the first model, there is no need to simulate the averaged conductivity tensor since the meshes coincide with the boundaries

of the layers. But the axial component of the magnetic field is a combination of the field generated by an x-directed source and a z-directed source. In the second model, the meshes do not coincide with the formation boundaries any longer, so we need to calculate the averaged conductivity tensor for all the cells. It should be noted that the conductivity tensors for each cell in the original principle coordinate system x-y-z should be transformed to the new coordinate system x'-y'-z' before they are used to get the averaged conductivity tensors. The transformation can be performed by multiplying the original conductivity tensor with a rotation matrix $\mathbf{R}$,

$$\bar{\sigma}' = \mathbf{R}^T \mathrm{diag}\left(\sigma_{xx}, \sigma_{yy}, \sigma_{zz}\right) \mathbf{R} \tag{17}$$

The rotation matrix R can be expressed by

$$R = \begin{bmatrix} \cos\theta\cos\phi & -\sin\phi & sin\theta\cos\phi \\ \cos\theta\sin\phi & \cos\phi & \sin\theta\sin\phi \\ -\sin\theta & 0 & \cos\theta \end{bmatrix} \tag{18}$$

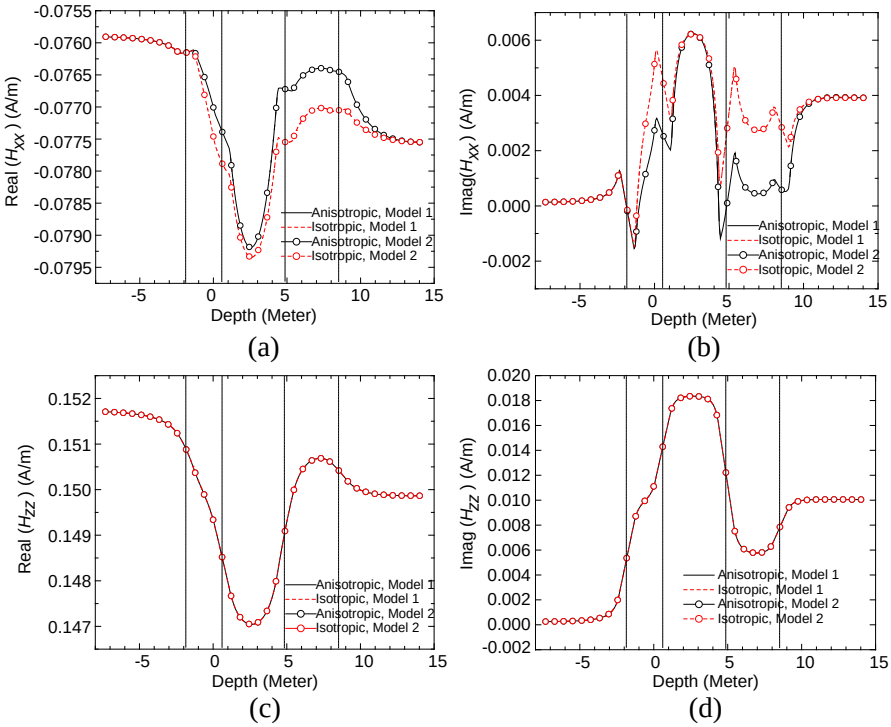

Figure 6. The calculated magnetic field from the two models. (a) Real (H_{xx}). (b) Imag (H_{xx}). (c) Real (H_{zz}). (d) Imag (H_{zz}).

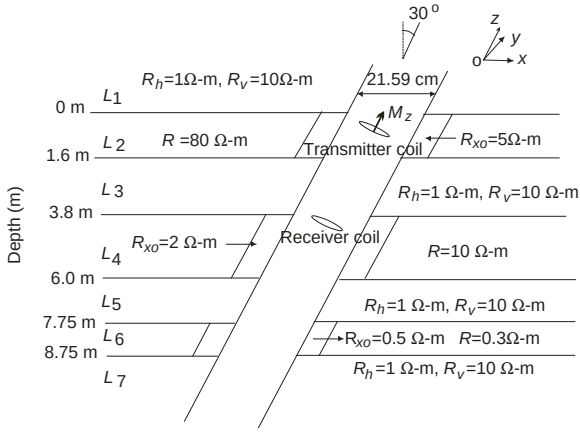

Figure 7. Geometry of a 7-layer anisotropic model.

where θ and ϕ are the two Euler angles corresponding to the dip and strike angles of the laminations. After rotation, the conductivity tensor will be a full tensor in the coordinate system x'-y'-z' in stead of a diagonal tensor in the original coordinate system x-y-z. Figure 6 shows the calculated magnetic field H_{xx} (both the transmitter coil and receiver coils are in the x direction) and H_{zz} (both the transmitter and receiver coils are in the y direction) at different vertical depth for a pair of transmitter and receiver spaced by 1.016 m and working at 20 kHz. Perfect agreement is observed between the results from the two different models, verifying the implementation of finite-difference method and the averaged conductivity tensor calculation.

In Figure 6, besides the results for the anisotropic case, we also present the H_{xx} and H_{zz} for the isotropic case, namely, Layer 2 and Layer 4 are also isotropic with resistivity being 1.0 ohm-m and 1.9 ohm-m, respectively. From Figures 6(c) and (d), we can see that the z-directed coupling H_{zz} are the same in the isotropic and anisotropic cases, implying that H_{zz} has no sensitivity to the vertical resistivity. On the contrary, Figures 6(a) and (b) shows that the x-directed coupling H_{xx} can detect the anisotropy property of the media.

Next, we consider a 7-layer anisotropic formation model as shown in Figure 7. The medium in Layer 1, 3, 5 and 7 is anisotropic and has a horizontal resistivity of 1 ohm-m and a vertical resistivity of 10 ohm-m. There are invasions in Layer 2, 4 and 6. Diameters of the borehole and invasion are 21.59 cm and 30.48 cm, respectively. The mud resistivity in the borehole is 0.4 ohm-m. Other parameters are given in the figure. We use a tool consisting of three collocated orthogonal transmitter

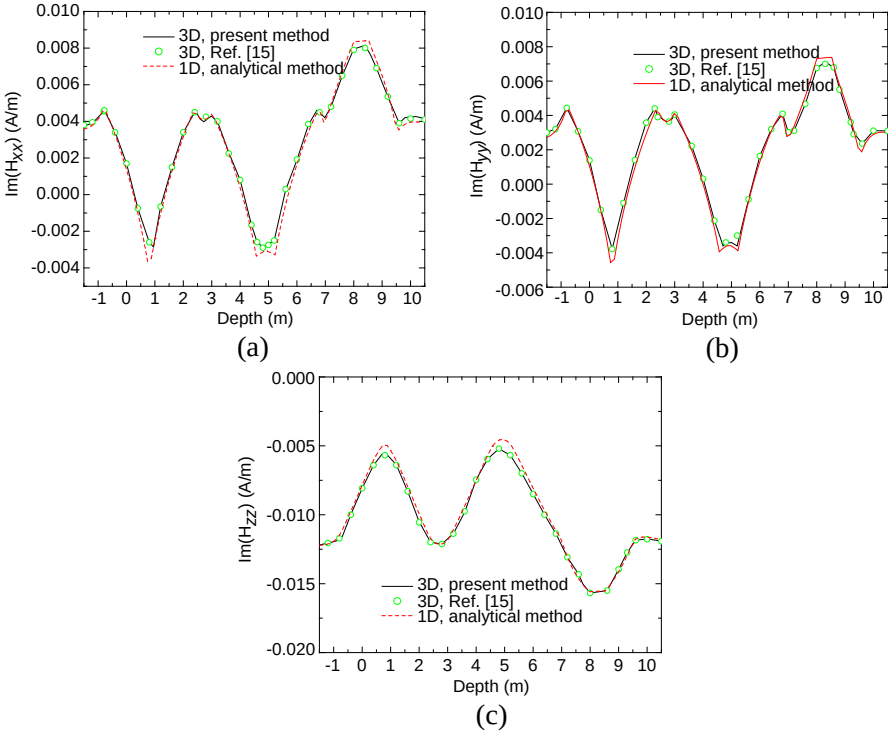

Figure 8. Comparison of the imaginary part of the magnetic field response of a 2-coil triaxial tool at 100 kHz. (a) H_{xx}. (b) H_{yy}. (c) H_{zz}.

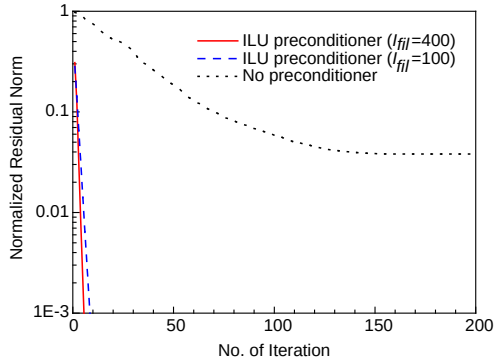

Figure 9. Convergence comparison with/without the preconditioner.

coils and three collocated orthogonal receiver coils to measure the magnetic field profile of the model. The transmitter and receiver coils are oriented at the x-, y- and z-direction. The dipping angle (the angle between the tool axis and the normal to the layer boundaries) is 30°. The spacing between the transmitter and receiver is 1.8 m. Figure 8 shows the calculated imaginary part of the H_{xx}, H_{yy} and H_{zz} responses at 100 kHz. The results from [15] are also presented in the figure for comparison. Good agreements are observed, validating the present 3D FDM code. In these figures, we also present the 1D result calculated by an analytical method [22] with the borehole and invasion neglected. It can be seen that the in the layers where there are no invasions, the 1D and 3D results are very close to each other since the borehole effect is not obvious in this case. However, in Layers 2, 4 and 6 where invasions exist, the 1D and 3D results have discrepancy, implying that 3D simulation is necessary to get accurate results and more information of surrounding media.

In Figure 9, we compare the convergence rates of the linear system with and without the ILU preconditioner. It is observed that without preconditioner, a normalized residual norm (NRN) of 1% cannot be achieved even after 200 iterations. However, with preconditioner, a NRN of 0.1% can be achieved in only 6 iterations for $I_{fil} = 400$ or 9 iterations for $I_{fil} = 100$. I_{fil} represents the number of elements in the ith row of the matrix L and U to be kept to construct the precondition matrix. Large I_{fil} means faster convergence but more memory requirements. Therefore the choice of I_{fil} must be a good compromise between the memory and convergence.

As an application of arbitrarily oriented coil antennas, we consider an example as shown in Figure 10. A transmitter-receiver pair spaced 2.4384 m is located in a 3-layer media. The center layer is 6.096 m thick and has a resistivity of 20 ohm-m. The upper and lower layer has a resistivity of 2 and 5 ohm-m, respectively. The tool (transmitter-

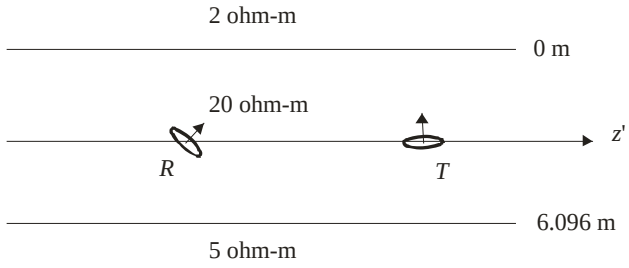

Figure 10. A tilted transmitter-receiver pair in a 3-layer media.

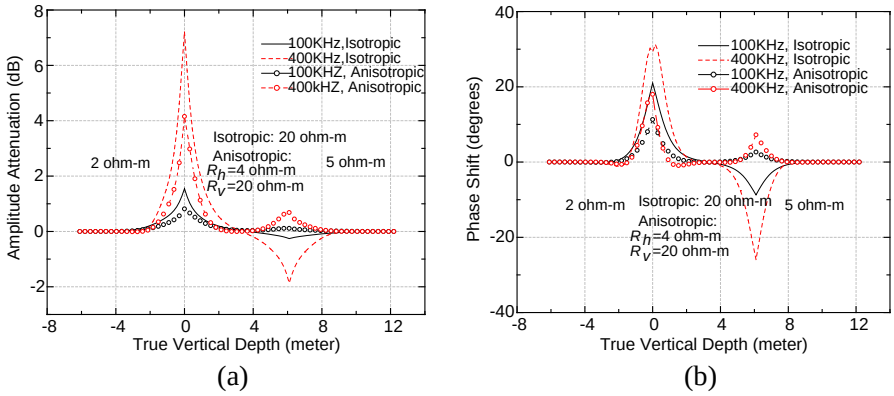

Figure 11. The response of a tilted transmitter-receiver pair in a 3-layer isotropic/anisotropic media. (a) Amplitude attenuation. (b) Phase shift.

receiver pair) is oriented parallel to the boundary, simulating a 90° horizontal well. The transmitter coil is pointed along the z' axis while the receiver is pointed at 45° with respective to the z' axis and rotates around the z' axis in the measurement. Figure 11 shows the amplitude attenuation and phase shift of the response (the ratio of the received signal when the receiver is pointed 45° and −45° degree) as a function of the true vertical depth at 100 kHz and 400 kHz. We can observe the following fact from Figure 11. First, the peak values of both the amplitude ratio and phase shift appear at the boundaries, determining the boundaries of different media. Second, the peak values increase as the frequency increases. Furthermore, when the tool approaches a more conductive layer from below, the directional phase shift and attenuation are positive. On the contrary, when the tool approaches a more conductive layer from above, the directional phase shift and attenuation are negative. This is a very important application in geosteering. The polarity can be used while drilling as a simple indicator to determine whether the directional driller should steer up or down. In Figure 11, we also present the results of an anisotropic case for comparison, in which the center layer has a horizontal resistivity of 4 ohm-m and a vertical resistivity of 20 ohm-m. From the figure, we can see that the existing of the anisotropy in the center layer changes the polarity of the phase shift and attenuation, as shown by the dotted curves between 6–8 m.

4. CONCLUSION

In this paper, we presented a 3-D finite-difference simulation for the electromagnetic field generated by arbitrarily oriented coil antennas in complicated underground anisotropic media. The method is applied to predict and study the electromagnetic response of triaxial induction tools in multi-layered dipping anisotropic formations. The results obtained by the present method are compared with the 1-D results from a transmission line theory. It is concluded that 1-D simulation shows obvious discrepancy with 3D simulation results in layers with invasions and the discrepancy becomes larger as the invasion extends deeper in the formation. This discrepancy also increases when the shoulder-bed is anisotropic. Therefore, to fully understand the effects of the borehole and invasions in a complicated multi-layered anisotropic formation, the full 3D simulation is necessary although it is slower than the 1D analytical simulation. The method can also be used to the simulation and design of geosteering drilling tools.

APPENDIX A.

Using a 13-point centered finite-difference stencil to approximate the curl-curl operators in (6) and applying a conductivity averaging scheme, (6) can be converted into a set of linear equations for the x-, y- and z-directed source

$$\begin{aligned}
&\left[E'_x\left(i+\frac{1}{2},j,k\right)-E'_x\left(i+\frac{1}{2},j-1,k\right)\right]/\Delta^y_{j-1}\Delta^y_{j-\frac{1}{2}}\\
&+\left[E'_x\left(i+\frac{1}{2},j,k\right)-E'_x\left(i+\frac{1}{2},j+1,k\right)\right]/\Delta^y_{j}\Delta^y_{j-\frac{1}{2}}\\
&+\left[E'_x\left(i+\frac{1}{2},j,k\right)-E'_x\left(i+\frac{1}{2},j,k-1\right)\right]/\Delta^z_{k-1}\Delta^z_{k-\frac{1}{2}}\\
&+\left[E'_x\left(i+\frac{1}{2},j,k\right)-E'_x\left(i+\frac{1}{2},j,k+1\right)\right]/\Delta^z_{k}\Delta^z_{k-\frac{1}{2}}\\
&+\left[E'_y\left(i,j-\frac{1}{2},k\right)-E'_y\left(i+1,j-\frac{1}{2},k\right)\right.\\
&\left.+E'_y\left(i+1,j+\frac{1}{2},k\right)-E'_y\left(i,j+\frac{1}{2},k\right)\right]/\Delta^x_{i}\Delta^y_{j-\frac{1}{2}}\\
&+\left[E'_z\left(i,j,k-\frac{1}{2}\right)-E'_z\left(i+1,j,k-\frac{1}{2}\right)\right.
\end{aligned}$$

$$
\begin{aligned}
&+E'_z\left(i+1,j,k+\frac{1}{2}\right)-E'_z\left(i,j,k+\frac{1}{2}\right)\Big]/\Delta_i^x\Delta_{k-\frac{1}{2}}^z\\
&+\frac{j\omega\mu_0E'_x\left(i+\frac{1}{2},j,k\right)}{\Delta_{j-\frac{1}{2}}^y\Delta_{k-\frac{1}{2}}^z}\left[\frac{1}{2}\Delta_{k-1}^z\left(\frac{1}{2}\Delta_{j-1}^y\sigma_{xx}^{[i,j-1,k-1]}+\frac{1}{2}\Delta_j^y\sigma_{xx}^{[i,j,k-1]}\right)\right.\\
&\left.+\frac{1}{2}\Delta_k^z\left(\frac{1}{2}\Delta_{j-1}^y\sigma_{xx}^{[i,j-1,k]}+\frac{1}{2}\Delta_j^y\sigma_{xx}^{[i,j,k]}\right)\right]\\
&+\frac{j\omega\mu_0}{\Delta_{j-\frac{1}{2}}^y\Delta_{k-\frac{1}{2}}^z}\left[\frac{\left(E'_y\left(i,j-\frac{1}{2},k\right)+E'_y\left(i+1,j-\frac{1}{2},k\right)\right)}{2/\left(\frac{1}{2}\Delta_{j-1}^y\right)\left(\frac{1}{2}\Delta_{k-1}^z\sigma_{xy}^{[i,j-1,k-1]}+\frac{1}{2}\Delta_k^z\sigma_{xy}^{[i,j-1,k]}\right)}\right.\\
&\left.+\frac{\left(E'_y\left(i,j+\frac{1}{2},k\right)+E'_y\left(i+1,j+\frac{1}{2},k\right)\right)}{2/\left(\frac{1}{2}\Delta_j^y\right)\left(\frac{1}{2}\Delta_{k-1}^z\sigma_{xy}^{[i,j,k-1]}+\frac{1}{2}\Delta_k^z\sigma_{xy}^{[i,j,k]}\right)}\right]\\
&+\frac{j\omega\mu_0}{\Delta_{j-\frac{1}{2}}^y\Delta_{k-\frac{1}{2}}^z}\left[\frac{\left(E'_z\left(i,j,k-\frac{1}{2}\right)+E'_z\left(i+1,j,k-\frac{1}{2}\right)\right)}{2/\left(\frac{1}{2}\Delta_{k-1}^z\right)\left(\frac{1}{2}\Delta_{j-1}^y\sigma_{xz}^{[i,j-1,k-1]}+\frac{1}{2}\Delta_j^y\sigma_{xz}^{[i,j,k-1]}\right)}\right.\\
&\left.+\frac{\left(E'_z\left(i,j,k+\frac{1}{2}\right)+E'_z\left(i+1,j,k+\frac{1}{2}\right)\right)}{2\Big/\left(\frac{1}{2}\Delta_k^z\right)\left(\frac{1}{2}\Delta_{j-1}^y\sigma_{xz}^{[i,j-1,k]}+\frac{1}{2}\Delta_j^y\sigma_{xz}^{[i,j,k]}\right)}\right]\\
&=\frac{-j\omega\mu_0}{\Delta_{j-\frac{1}{2}}^y\Delta_{k-\frac{1}{2}}^z}\left\{\left[\frac{1}{2}\Delta_{k-1}^z\left(\frac{1}{2}\Delta_{j-1}^y\left(\sigma_{xx}^{[i,j-1,k-1]}-\sigma_0\right)\right.\right.\right.\\
&\left.+\frac{1}{2}\Delta_j^y\left(\sigma_{xx}^{[i,j,k-1]}-\sigma_0\right)\right)+\frac{1}{2}\Delta_k^z\left(\frac{1}{2}\Delta_{j-1}^y\left(\sigma_{xx}^{[i,j-1,k]}-\sigma_0\right)\right.\\
&\left.\left.\left.+\frac{1}{2}\Delta_j^y\left(\sigma_{xx}^{[i,j,k]}-\sigma_0\right)\right)\right]E_0^x\left(i+\frac{1}{2},j,k\right)\\
&+\left[\frac{1}{2}\Delta_{k-1}^z\left(\frac{1}{2}\Delta_{j-1}^y\sigma_{xy}^{[i,j-1,k-1]}+\frac{1}{2}\Delta_j^y\sigma_{xy}^{[i,j,k-1]}\right)\right.\\
&\left.+\frac{1}{2}\Delta_k^z\left(\frac{1}{2}\Delta_{j-1}^y\sigma_{xy}^{[i,j-1,k]}+\frac{1}{2}\Delta_j^y\sigma_{xy}^{[i,j,k]}\right)\right]E_0^y\left(i+\frac{1}{2},j,k\right)\\
&+\left[\frac{1}{2}\Delta_{k-1}^z\left(\frac{1}{2}\Delta_{j-1}^y\sigma_{xz}^{[i,j-1,k-1]}+\frac{1}{2}\Delta_j^y\sigma_{xz}^{[i,j,k-1]}\right)\right.\\
&\left.\left.+\frac{1}{2}\Delta_k^z\left(\frac{1}{2}\Delta_{j-1}^y\sigma_{xz}^{[i,j-1,k]}+\frac{1}{2}\Delta_j^y\sigma_{xz}^{[i,j,k]}\right)\right]E_0^z\left(i+\frac{1}{2},j,k\right)\right\} \qquad \text{(A1)}
\end{aligned}
$$

$$
\begin{aligned}
&\left[E'_y\left(i,j+\frac{1}{2},k\right)-E'_y\left(i,j+\frac{1}{2},k-1\right)\right]/\Delta^z_{k-1}\Delta^z_{k-\frac{1}{2}}\\
&+\left[E'_y\left(i,j+\frac{1}{2},k\right)-E'_y\left(i,j+\frac{1}{2},k+1\right)\right]/\Delta^z_{k}\Delta^z_{k-\frac{1}{2}}\\
&+\left[E'_y\left(i,j+\frac{1}{2},k\right)-E'_y\left(i-1,j+\frac{1}{2},k\right)\right]/\Delta^x_{i-1}\Delta^x_{i-\frac{1}{2}}\\
&+\left[E'_y\left(i,j+\frac{1}{2},k\right)-E'_y\left(i+1,j+\frac{1}{2},k\right)\right]/\Delta^x_{i}\Delta^x_{i-\frac{1}{2}}\\
&+\left[E'_x\left(i-\frac{1}{2},j,k\right)-E'_x\left(i-\frac{1}{2},j+1,k\right)\right.\\
&\left.+E'_x\left(i+\frac{1}{2},j+1,k\right)-E'_x\left(i+\frac{1}{2},j,k\right)\right]/\Delta^x_{i-\frac{1}{2}}\Delta^y_{j}\\
&+\left[E'_z\left(i,j,k-\frac{1}{2}\right)-E'_z\left(i,j+1,k-\frac{1}{2}\right)\right.\\
&\left.+E'_z\left(i,j+1,k+\frac{1}{2}\right)-E'_z\left(i,j,k+\frac{1}{2}\right)\right]/\Delta^y_{j}\Delta^z_{k-\frac{1}{2}}\\
&+\frac{j\omega\mu_0 E'_y\left(i,j+\frac{1}{2},k\right)}{\Delta^x_{i-\frac{1}{2}}\Delta^z_{k-\frac{1}{2}}}\left[\frac{1}{2}\Delta^z_{k-1}\left(\frac{1}{2}\Delta^x_{i-1}\sigma^{[i-1,j,k-1]}_{yy}+\frac{1}{2}\Delta^x_{i}\sigma^{[i,j,k-1]}_{yy}\right)\right.\\
&\left.+\frac{1}{2}\Delta^z_{k}\left(\frac{1}{2}\Delta^x_{i-1}\sigma^{[i-1,j,k]}_{yy}+\frac{1}{2}\Delta^x_{i}\sigma^{[i,j,k]}_{yy}\right)\right]\\
&+\frac{j\omega\mu_0}{\Delta^x_{i-\frac{1}{2}}\Delta^z_{k-\frac{1}{2}}}\left[\frac{\left(E'_x\left(i-\frac{1}{2},j,k\right)+E'_x\left(i-\frac{1}{2},j+1,k\right)\right)}{2/\left(\frac{1}{2}\Delta^x_{i-1}\right)\left(\frac{1}{2}\Delta^z_{k-1}\sigma^{[i-1,j,k-1]}_{yx}+\frac{1}{2}\Delta^z_{k}\sigma^{[i-1,j,k]}_{yx}\right)}\right.\\
&\left.+\frac{\left(E'_x\left(i+\frac{1}{2},j,k\right)+E'_x\left(i+\frac{1}{2},j+1,k\right)\right)}{2/\left(\frac{1}{2}\Delta^x_{i}\right)\left(\frac{1}{2}\Delta^z_{k-1}\sigma^{[i,j,k-1]}_{yx}+\frac{1}{2}\Delta^z_{k}\sigma^{[i,j,k]}_{yx}\right)}\right]\\
&+\frac{j\omega\mu_0}{\Delta^x_{i-\frac{1}{2}}\Delta^z_{k-\frac{1}{2}}}\left[\frac{\left(E'_z\left(i,j,k-\frac{1}{2}\right)+E'_z\left(i,j+1,k-\frac{1}{2}\right)\right)}{2/\left(\frac{1}{2}\Delta^z_{k-1}\right)\left(\frac{1}{2}\Delta^x_{i-1}\sigma^{[i-1,j,k-1]}_{yz}+\frac{1}{2}\Delta^x_{i}\sigma^{[i,j,k-1]}_{yz}\right)}\right.\\
&\left.+\frac{\left(E'_z\left(i,j,k+\frac{1}{2}\right)+E'_z\left(i,j+1,k+\frac{1}{2}\right)\right)}{2/\left(\frac{1}{2}\Delta^z_{k}\right)\left(\frac{1}{2}\Delta^x_{i-1}\sigma^{[i-1,j,k]}_{yz}+\frac{1}{2}\Delta^x_{i}\sigma^{[i,j,k]}_{yz}\right)}\right]\\
&=\frac{-j\omega\mu_0}{\Delta^x_{i-\frac{1}{2}}\Delta^z_{k-\frac{1}{2}}}\left\{\left[\frac{1}{2}\Delta^z_{k-1}\left(\frac{1}{2}\Delta^x_{i-1}\left(\sigma^{[i-1,j,k-1]}_{yy}-\sigma_0\right)+\frac{1}{2}\Delta^x_{i}\left(\sigma^{[i,j,k-1]}_{yy}-\sigma_0\right)\right)\right.\right.
\end{aligned}
$$

$$
\begin{aligned}
&+\frac{1}{2}\Delta_k^z\left(\frac{1}{2}\Delta_{i-1}^x\left(\sigma_{yy}^{[i-1,j,k]}-\sigma_0\right)+\frac{1}{2}\Delta_i^x\left(\sigma_{yy}^{[i,j,k]}-\sigma_0\right)\right)\Bigg]E_0^y\left(i,j+\frac{1}{2},k\right)\\
&+\left[\frac{1}{2}\Delta_{k-1}^z\left(\frac{1}{2}\Delta_{i-1}^x\sigma_{yx}^{[i-1,j,k-1]}+\frac{1}{2}\Delta_i^x\sigma_{yx}^{[i,j,k-1]}\right)\right.\\
&\left.+\frac{1}{2}\Delta_k^z\left(\frac{1}{2}\Delta_{i-1}^x\sigma_{yx}^{[i-1,j,k]}+\frac{1}{2}\Delta_i^x\sigma_{yx}^{[i,j,k]}\right)\right]E_0^x\left(i,j+\frac{1}{2},k\right)\\
&+\left[\frac{1}{2}\Delta_{k-1}^z\left(\frac{1}{2}\Delta_{i-1}^x\sigma_{yz}^{[i-1,j,k-1]}+\frac{1}{2}\Delta_i^x\sigma_{yz}^{[i,j,k-1]}\right)\right.\\
&\left.+\frac{1}{2}\Delta_k^z\left(\frac{1}{2}\Delta_{i-1}^x\sigma_{yz}^{[i-1,j,k]}+\frac{1}{2}\Delta_i^x\sigma_{yz}^{[i,j,k]}\right)\right]E_0^z\left(i,j+\frac{1}{2},k\right)\Bigg\} \qquad \text{(A2)}\\
&\left[E_z'\left(i,j,k+\frac{1}{2}\right)-E_z'\left(i-1,j,k+\frac{1}{2}\right)\right]/\Delta_{i-1}^x\Delta_{i-\frac{1}{2}}^x\\
&+\left[E_z'\left(i,j,k+\frac{1}{2}\right)-E_z'\left(i+1,j,k+\frac{1}{2}\right)\right]/\Delta_i^x\Delta_{i-\frac{1}{2}}^x\\
&+\left[E_z'\left(i,j,k+\frac{1}{2}\right)-E_z'\left(i,j-1,k+\frac{1}{2}\right)\right]/\Delta_{j-1}^y\Delta_{j-\frac{1}{2}}^y\\
&+\left[E_z'\left(i,j,k+\frac{1}{2}\right)-E_z'\left(i,j+1,k+\frac{1}{2}\right)\right]/\Delta_j^y\Delta_{j-\frac{1}{2}}^y\\
&+\left[E_x'\left(i-\frac{1}{2},j,k\right)-E_x'\left(i-\frac{1}{2},j,k+1\right)\right.\\
&\left.+E_x'\left(i+\frac{1}{2},j,k+1\right)-E_x'\left(i+\frac{1}{2},j,k\right)\right]/\Delta_{i-\frac{1}{2}}^x\Delta_k^z\\
&+\left[E_y'\left(i,j-\frac{1}{2},k\right)-E_y'\left(i,j-\frac{1}{2},k+1\right)\right.\\
&\left.+E_y'\left(i,j+\frac{1}{2},k+1\right)-E_y'\left(i,j+\frac{1}{2},k\right)\right]/\Delta_{j-\frac{1}{2}}^y\Delta_k^z\\
&+\frac{j\omega\mu_0E_z'\left(i,j,k+\frac{1}{2}\right)}{\Delta_{i-\frac{1}{2}}^x\Delta_{j-\frac{1}{2}}^y}\left[\frac{1}{2}\Delta_{j-1}^y\left(\frac{1}{2}\Delta_{i-1}^x\sigma_{zz}^{[i-1,j-1,k]}+\frac{1}{2}\Delta_i^x\sigma_{zz}^{[i,j-1,k]}\right)\right.\\
&\left.+\frac{1}{2}\Delta_j^y\left(\frac{1}{2}\Delta_{i-1}^x\sigma_{zz}^{[i-1,j,k]}+\frac{1}{2}\Delta_i^x\sigma_{zz}^{[i,j,k]}\right)\right]\\
&+\frac{j\omega\mu_0}{\Delta_{i-\frac{1}{2}}^x\Delta_{j-\frac{1}{2}}^y}\left[\frac{\left(E_x'\left(i-\frac{1}{2},j,k\right)+E_x'\left(i-\frac{1}{2},j,k+1\right)\right)}{2/\left(\frac{1}{2}\Delta_{i-1}^x\right)\left(\frac{1}{2}\Delta_{j-1}^y\sigma_{zx}^{[i-1,j-1,k]}+\frac{1}{2}\Delta_j^y\sigma_{zx}^{[i-1,j,k]}\right)}\right.
\end{aligned}
$$

$$+\frac{\left(E'_x\left(i+\frac{1}{2},j,k\right)+E'_x\left(i+\frac{1}{2},j,k+1\right)\right)}{2/\left(\frac{1}{2}\Delta_i^x\right)\left(\frac{1}{2}\Delta_{j-1}^y\sigma_{zx}^{[i,j-1,k]}+\frac{1}{2}\Delta_j^y\sigma_{zx}^{[i,j,k]}\right)}\Bigg]$$

$$+\frac{j\omega\mu_0}{\Delta_{i-\frac{1}{2}}^x\Delta_{j-\frac{1}{2}}^y}\Bigg[\frac{\left(E'_y\left(i,j-\frac{1}{2},k\right)+E'_y\left(i,j-\frac{1}{2},k+1\right)\right)}{2/\left(\frac{1}{2}\Delta_{j-1}^y\right)\left(\frac{1}{2}\Delta_{i-1}^x\sigma_{zy}^{[i-1,j-1,k]}+\frac{1}{2}\Delta_i^x\sigma_{zy}^{[i,j-1,k]}\right)}$$

$$+\frac{\left(E'_y\left(i,j+\frac{1}{2},k\right)+E'_x\left(i,j+\frac{1}{2},k+1\right)\right)}{2/\left(\frac{1}{2}\Delta_j^y\right)\left(\frac{1}{2}\Delta_{i-1}^x\sigma_{zy}^{[i-1,j,k]}+\frac{1}{2}\Delta_i^x\sigma_{zy}^{[i,j,k]}\right)}\Bigg]$$

$$=\frac{-j\omega\mu_0}{\Delta_{i-\frac{1}{2}}^x\Delta_{j-\frac{1}{2}}^y}\Bigg\{\Bigg[\frac{1}{2}\Delta_{j-1}^y\Bigg(\frac{1}{2}\Delta_{i-1}^x\Big(\sigma_{zz}^{[i-1,j-1,k]}-\sigma_0\Big)+\frac{1}{2}\Delta_i^x\Big(\sigma_{zz}^{[i,j-1,k]}-\sigma_0\Big)\Bigg)$$

$$+\frac{1}{2}\Delta_j^y\Bigg(\frac{1}{2}\Delta_{i-1}^x\Big(\sigma_{zz}^{[i-1,j,k]}-\sigma_0\Big)+\frac{1}{2}\Delta_i^x\Big(\sigma_{zz}^{[i,j,k]}-\sigma_0\Big)\Bigg)\Bigg]E_0^z\left(i,j,k+\frac{1}{2}\right)$$

$$+\Bigg[\frac{1}{2}\Delta_{j-1}^y\left(\frac{1}{2}\Delta_{i-1}^x\sigma_{zx}^{[i-1,j-1,k]}+\frac{1}{2}\Delta_i^x\sigma_{zx}^{[i,j-1,k]}\right)$$

$$+\frac{1}{2}\Delta_j^y\left(\frac{1}{2}\Delta_{i-1}^x\sigma_{zx}^{[i-1,j,k]}+\frac{1}{2}\Delta_i^x\sigma_{zx}^{[i,j,k]}\right)\Bigg]E_0^x\left(i,j,k+\frac{1}{2}\right)$$

$$+\Bigg[\frac{1}{2}\Delta_{j-1}^y\left(\frac{1}{2}\Delta_{i-1}^x\sigma_{zy}^{[i-1,j-1,k]}+\frac{1}{2}\Delta_i^x\sigma_{zy}^{[i,j-1,k]}\right)$$

$$+\frac{1}{2}\Delta_j^y\left(\frac{1}{2}\Delta_{i-1}^x\sigma_{zy}^{[i-1,j,k]}+\frac{1}{2}\Delta_i^x\sigma_{zy}^{[i,j,k]}\right)\Bigg]E_0^y\left(i,j,k+\frac{1}{2}\right)\Bigg\} \quad \text{(A3)}$$

REFERENCES

1. Moran, J. H. and S. Gianzero, "Effects of formation anisotropy on resistivity-logging measurements," *Geophysics*, Vol. 44, 1266–1286, 1984.
2. Anderson, B. and S. K. Chang, "Synthetic induction logs by the finite element method," *The Log Analyst*, Vol. 23, 17–26, 1982.
3. Anderson, B., "Simulation of induction logging by the finite-element method," *Geophysics*, Vol. 49, 1943–1958, 1984.
4. Everett, M. E., E. A. Badea, L. C. Shen, G. A. Merchant, and C. J. Weiss, "3-D finite element analysis of induction logging in a dipping formation," *IEEE Trans. Geoscience and Remote Sensing*, Vol. 39, 2244–2252, 2001.
5. Han, W. S., "3D finite element simulation method of induction and MWD tools," Ph.D. Dissertation, University of Houston, 2004.

6. Zhdanov, M. S., S. K. Lee, and K. Yoshioka, "Integral equation method for 3D modeling of electromagnetic fields in complex structures within homogeneous background conductivity," *Geophysics*, Vol. 67, 333–345, 2006.
7. Fang, S., G. Z. Gao, and C. Torres-Verdin, "Efficient 3D electromagnetic modeling in the presence of anisotropic conductive media, using integral equations," *Exploration Geophysics*, Vol. 37, 239–244, 2006.
8. Nie, X. C., N. Yuan, and R. Liu, "Simulation of LWD tool response using a fast integral equation method," *IEEE Trans. on Geoscience and Remote Sensing,* Vol. 48, No. 1, 72–81, Jan. 2010.
9. Weiss, C. J. and G. A. Newman, "Electromagnetic induction in a fully 3-D anisotropic earth," *Geophysics*, Vol. 67, No. 4, 1104–1114, Jul.–Aug. 2002.
10. Wang, T. and S. Fang, "3-D electromagnetic anisotropic modeling using finite difference," *Geophysics*, Vol. 66, No. 5, 1386–1398, Sept.–Oct. 2001.
11. Davydycheva, S., V. Druskin, and T. Habashy, "An efficient finite-difference scheme for electromagnetic logging in 3D anisotropic inhomogeneous media," *Geophysics*, Vol. 68, No. 5, 1525–1536, Sept.–Oct. 2003.
12. Newman, G. A. and D. L. Alumbaugh, "Three-dimensional induction logging problems, Part 2: A finite-difference solution," *Geophysics*, Vol. 67, No. 2, 484–491, Mar.–Apr. 2002.
13. Streich, R., "3D finite-difference frequency-domain modeling of controlled-source electromagnetic data: Direct solution and optimization for high accuracy," *Geophysics,* Vol. 74, F95–F105, 2009.
14. Davydycheva, S., D. Homan, and G. Minerbo, "Triaxial induction tool with electrode sleeve: FD modeling in 3D geometries," *Journal of Applied Geophysics*, Vol. 67, 98–108, 2009.
15. Hou, J. S., R. K. Mallan, and C. Torres-Verdin, "Finite-difference simulation of borehole EM measurements in 3D anisotropic media using coupled scalar-vector potentials," *Geophysics*, Vol. 71, No. 5, G225–G233, Sept.–Oct. 2006.
16. Novo, M. S., L. C. da Silva, and F. L. Teixeira, "Finite volume modeling of borehole electromagnetic logging in 3-D anisotropic formations using coupled scalar-vector potentials," *IEEE Antennas and Wireless Propagation Letters*, 549–552, 2007.
17. Novo, M. S., L. C. da Silva, and F. L. Teixeira, "Comparison of coupled-potentials and field-based finite-volume techniques for

modeling of borehole EM tools," *IEEE Geoscience and Remote Sensing Letters*, Vol. 5, No. 2, Apr. 2008.

18. Saad, Y. and M. H. Schultz, "GMRES: A generalized minimal residual algorithm for solving nonsymmetric linear systems," *SIAM Journal of Sci. STAT. Comput.*, Vol. 7, No. 3, 856–869, 1986.
19. Saad, Y., "ILUT: A dual threshold incomplete LU factorization," *Numer. Linear Algebra Appl.*, Vol. 1, No. 4, 387–402, 1994.
20. Yuan, N., X. C. Nie, Y. B. Gan, T. S. Yeo, and L. W. Li, "Accurate analysis of conformal antenna arrays with finite and curved frequency selective surfaces," *Journal of Electromagnetic Waves and Applications,* Vol. 21, No. 13, 1745–1760, 2007.
21. Yee, K. S., "Numerical solution of initial boundary value problems involving Maxwell's equations in isotropic media," *IEEE Trans. Antennas Propagat.*, Vol. 14, No. 3, 302–307, Jan. 1984.
22. Yuan, N., X. C. Nie, and R. Liu, "Electromagnetic field response of triaxial induction logging tools in 1-D multi-layered anisotropic formations," *2010 IEEE AP-S International Symposium on Antennas and Propagation and 2010 USNC/URSI National Radio Science Meeting*, Toronto, ON, Canada, Jul. 11–17, 2010.